RSC Advances


This is an *Accepted Manuscript*, which has been through the Royal Society of Chemistry peer review process and has been accepted for publication.

*Accepted Manuscripts* are published online shortly after acceptance, before technical editing, formatting and proof reading. Using this free service, authors can make their results available to the community, in citable form, before we publish the edited article. This *Accepted Manuscript* will be replaced by the edited, formatted and paginated article as soon as this is available.

You can find more information about *Accepted Manuscripts* in the Information for Authors.

Please note that technical editing may introduce minor changes to the text and/or graphics, which may alter content. The journal's standard Terms & Conditions and the Ethical guidelines still apply. In no event shall the Royal Society of Chemistry be held responsible for any errors or omissions in this *Accepted Manuscript* or any consequences arising from the use of any information it contains.

ROYAL SOCIETY OF CHEMISTRY

www.rsc.org/advances

Cite this: DOI: 10.1039/x0xx00000x

# Fabrication of Flexible Reduced Graphene Oxide-$TiO_2$ Freestanding Films for Supercapacitor Application

Jinsu Kim[a], Wai-Hwa Khoh[a], Boon-Hong Wee[a], and Jong-Dal Hong*[a,b]

Received 00th January 2012,
Accepted 00th January 2012

DOI: 10.1039/x0xx00000x

www.rsc.org/

This paper described the fabrication of a flexible composite film electrode (rGT) composed of the reduced graphene oxide (rGO) and $TiO_2$ in an aligned stacking structure of rGO/$TiO_2$ layers using a simple vacuum-assisted filtration method. The SEM images of rGO and rGT films indicate that the rGO film (d = 5.6±0.5 μm) was highly expanded into a layered structure of the rGT (d = 7.2±0.5 μm) intercalated by the $TiO_2$ nanoparticles, which prevent the interlayer stacking of graphene sheets. The intensities of C-O and C=O bonding peaks in X-ray photoelectron spectra of rGT films, decreased dramatically, as the reduction temperature was increased from 100 to 600 °C, indicating almost complete removal of the oxygenated functional groups. Hence, the electrochemical property of rGT film electrode significantly relied on the reduction temperature of graphene oxide (GO)-$TiO_2$ film. The $rGT_{600}$ electrode (annealed at 600 °C) in 1.0 M $Na_2SO_4$ aqueous electrolyte exhibited the specific capacitance of 286 F/g in addition to the excellent cycling stability with 93% capacitance retention after 1000 continuous charge/discharge cycles at 1 A/g. The specific capacitance of $rGT_{600}$ electrode in the expanded interlayer stacking structure of rGO and $TiO_2$ particles was by 63% higher than that of the three-dimensional $TiO_2$-graphene hydrogel electrode (175 F/g, 1A/g) prepared using one-step hydrothermal approach.[1] The modification in the preparation of the composite films comprising rGO sheets and $TiO_2$ particles optimized the supercapacitor electrodes into the expanded interlayer stacking rGO/$TiO_2$ structure, exhibiting the excellent electrochemical performances, which are required for the development of advanced micro-size and flexible electrodes in energy storage devises.

## 1. Introduction

The development of highly efficient energy storage devices has attracted great interest due to the drastic depletion of fossil fuel reserves and the environmental pollution caused by the excessive use of fossil fuels. Furthermore, the invention of small, flexible, and portable electronic devices have triggered the development of high performance micro- or nanoscale power sources.[2,3] Among different types of energy storage devices, supercapacitors are attractive systems, which bridge the gap between batteries and conventional capacitors, because of their higher power density and longer life cycle than batteries, as well as higher energy density than conventional capacitor.[4,5] Supercapacitors can be classified into two basic types according to their charge storage mechanism: electrical double layer capacitance (EDLC) and pseudocapacitance. The EDLC is generated from the charges that built up electrostatically at the interface of electrode and electrolyte, whereas the pseudocapacitance is generated from the rapid faradaic reactions that occur on either the surface or bulk of electrode.[5,6] In general, highly porous carbon materials (activated carbon, carbon nanotube, graphene) are used for charge storage via the formation of the EDL at the electrode/electrolyte interface. Almost unlimited number of charge-discharge cycle can be expected due to the absence of electrochemical degradation in the electrode. Pseudocapacitors that use reactive materials including transition metal oxides and conducting polymers are able to store charges via redox reaction. Pseudocapacitances normally suffer from low power density and poor electrochemical stability due to the irreversible redox processes.[6-12] Therefore, current research has been focused mainly on the development of supercapacitor with hybrid electrode containing redox active materials and porous carbon materials for achieving both high power density and energy density.[13,14]

Graphene, a two-dimensional sheet of $sp^2$-hybridized carbon, is one of the most attractive materials for energy storage devices due to its extraordinary thermal, mechanical, and electrical properties.[15] Reduced graphene oxide (rGO), which is generated from graphite oxide, has been a promising route for mass production of chemically modified graphene sheets.[16,17] Graphene oxide (GO) obtained via simple and cheap solution processes is hydrophilic due to the presence of various oxygenated functional groups, and forms stable aqueous colloids.[15,17,18] GO is electrically insulating material due to disrupted $sp^2$ carbon bonding networks, and, thus, not suitable for supercapacitor applications. Chemical or high temperature treatment of is required to convert it to the electrically conductive rGO.[19] However, rGO inclined to restack and aggregate due to the strong hydrophobic and π-π interactions between rGO sheets, which lead to reduced

RSC Advances Accepted Manuscript

specific surface area, thereby resulting in poor capacitive performance.[20,21] The restacking of rGO sheets can be suppressed by incorporating secondary materials such as $RuO_2$.[5] polyaniline nano fibers,[22] and carbon black composites[23] for porous composite electrode. Titanium oxide ($TiO_2$) was investigated for the electrode material in energy storage devices due to the pseudocapacitance behavior, excellent chemical stability, eco friendliness, and low production cost.[1,24-27] However, the poor electrical conductivity of the $TiO_2$ has limited its use in many electronic applications[28] Incorporation of conductive rGO into $TiO_2$ electrode would overcome the shortcomings in the conductivity and mechanical flexibility of either rGO or $TiO_2$ electrode. Many methods have been proposed to prepare the graphene-$TiO_2$ hybrids composites for supercapacitor electrodes. For example, $TiO_2$ nanoparticles with particle sizes in the range of 8-15 nm were decorated over functionalized graphene by sol-gel methods.[29] Xiang and co-workers[24] synthesized rGO-$TiO_2$ round-shape nanoparticles and fiber-shape nanobelts using hydrothermal approach and studied the effect of the $TiO_2$ shape on the supercapacitor performance. Additionally, Graphene-$TiO_2$ hybrid nanostructure with uniformly distributed $TiO_2$ nanoparticles on the graphene surface was successfully synthesized using microwave-assisted method.[27] However, these rGO-$TiO_2$ electrodes required the use of poly(vinylidene fluoride) (PVDF) binder, which severely decreased the electrode conductivity and porosity, leading to poor capacitive performance.

The rapid development of portable and flexible electronic devices has triggered a concerted effort among researchers to develop high performance flexible energy storage devices. Recent studies related to the flexible supercapacitors have shown promising electrochemical performances particularly of those devices composed of carbon-based electrode.[30-33] For example, free-standing SWNT/PANi composite film(synthesized using in-situ electrochemical polymerization/degradation process)[30,31] could show high specific capacitance of 706 F/g in a three electrode system. A flexible asymmetric supercapacitor composed of graphene/carbon nanotube/$MnO_2$ (positive electrode) and graphene/carbon nanotube/polypyrrole (negative electrode) operating at a cell voltage of 1.6 V in aqueous electrolyte showed high energy density and power density of 22.8 Wh/kg and 860 W/kg, respectively.[32] In addition, 3D graphene hydrogel films used in a solid state flexible supercapacitor achieved high specific capacitance of 186 F/g at 1 A/g in polymer electrolyte.[33]

Here, we report the fabrication of a binder-free composite freestanding film composed of rGO and $TiO_2$ (rGT) for supercapacitor electrode, whereby $TiO_2$ particles were formed via the hydrolysis of $Ti(SO_4)_2$ on GO sheets. The resulting homogenous GO-$TiO_2$ dispersion was filtered using a vacuum-assisted filtration to form GO-$TiO_2$ (GT) film, which was converted to rGT during a thermal treatment at 600 $^oC$. These preparation procedures led to the optimization of the rGT electrode structure with an expanded stacking rGO/$TiO_2$ layers, exhibiting the highly improved electrochemical properties, compared to the one-step hydrothermal approach for three-dimensional (3D) $TiO_2$-graphene hydrogel electrode, which was developed by Zhang and co-workers.[1] Simultaneous reduction of GO and crystallization of $TiO_2$ is one of the optimal approaches as it provides good contact between the two materials with defined crystallized morphology.[34] The highly expanded layer-structured rGT electrode exhibited the specific capacitance of 286 F/g at a current density of 1 A/g, which was by 63% higher than that of the 3D $TiO_2$-graphene hydrogel electrode (175 F/g at 1 A/g).[1]

## 2. Experimental

### 2.1 Materials

Natural graphite powder (particle size < 20 μm), potassium permanganate ($KMnO_4$), potassium persulfate ($K_2S_2O_8$), titanium sulfate ($Ti(SO_4)_2$) and phosphorus pentoxide ($P_2O_5$) were purchased from sigma-Aldrich, and used as received. Concentrated sulfuric acid ($H_2SO_4$) was purchased from Daejung Chemicals (South Korea), and hydrochloric acid (HCl, 35%) and hydrogen peroxide ($H_2O_2$, 30%) were obtained from OCI Company Ltd. (Korea). Tin-doped indium oxide (ITO glass, 8 Ω $cm^{-1}$, d = 100 mm) was purchased from MEMC Electronic materials Inc.

### 2.2 Preparation of graphene oxide (GO)

GO solution was synthesized according to the modified Hummers method.[35] First, 10 mL of concentrated sulphuric acid ($H_2SO_4$) in 500 mL round bottom flask was heated to 80 °C, and then 0.9 g of potassium persulfate ($(NH_4)_2S_2O_8$) and 0.9 g phosphorus pentoxide ($P_2O_5$) were added into the solution while stirring. After stirring for 30 min, 1 g of graphite powder was added at 80 °C for 4.5 h. Upon being cooled to RT, the mixture was diluted with 250 mL of distilled water, and kept for 12 h at RT. The mixture was then filtrated, washed at least 5 times with distilled water, and dried in vacuum oven. The dried solid sample was added to 40 mL of concentrated sulphuric acid in 500 mL round bottom flask in an ice bath. Then, 5 g of potassium permanganate ($KMnO_4$) was slowly added into the mixture (5 g per 40 minutes) with keeping the temperature under 10 °C. The reaction mixture was heated at 35 °C for 2 h (a color change from black to greenish brown), and followed by dilution with 85 mL of DI water. (Caution: the temperature must be kept at < 35 °C throughout). After that, 250 mL of DI water and 10 mL of 30% aqueous hydrogen peroxide ($H_2O_2$) was added into the mixture. Bubbles were observed from the aqueous mixture along with a color change to brilliant yellow. Then, the mixture was allowed to settle for 12 h; the clear supernatant was removed and the sediment was washed with $H_2SO_4$ (5 wt%), $H_2O_2$ (0.5 wt%) and HCl (10 wt%) solutions, repeatedly. The dark yellow sediment was washed with DI water. This washing step was repeated,

RSC Advances Accepted Manuscript

until no layer separation was observed after centrifuging at 4000 rpm. Finally, the synthesized GO solution was dialyzed against DI water for 7 days, and dried in vacuum oven.

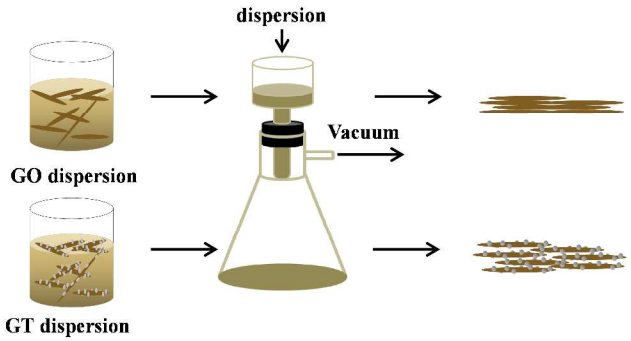


Fig 1. Schematic of the formation of GO film (top), and GT (bottom) film.

### 2.3 Preparation of reduced graphene oxide/titanium (rGT) composite films

The GT composite film was prepared based on the previous reports.[36,37] To prepare a GT dispersion, 20 mg of dried GO and 60 mg of $Ti(SO_4)_2$ were dispersed in 40 mL of DI water, and the mixture solution was stirred and heated at 60 °C for 24 h. In this procedure, $TiO_2$ nanoparticles were formed during the hydrolysis of $Ti(SO_4)_2$, and attached to GO sheet. The obtained product was centrifuged, and washed 5 times with distilled water, and then re-dispersed in the mixture of 20 mL of ethanol and 28 mL of DI water, and kept in an oven at 60 °C for 3 days. The composite sample was centrifuged, and washed with DI water at least 5 times to eliminate any impurities. Finally, the obtained GT composite was dispersed in 20 mL of distilled water. GT composite freestanding film was prepared by vacuum filtration of the 20 mL of composite solution through cellulose acetate membrane (50 mm diameter and 0.2 µm pore size), followed by peeling off from the membrane filter after drying, as shown in Fig. 1 The obtained-freestanding GTx (x = 100, 200, 300, 400, 500, and 600 °C) films were thermally reduced at various temperatures ranging from 100 to 600 °C in a tube furnace in an argon atmosphere with heating rate of 10 °C $min^{-1}$. GO film was also prepared using the same experimental procedure for comparison with the GT film.

### 2.4 Material characterization

The cross sectional view and surface morphology of the rGO and rGT films were investigated using field emission scanning electron microscopy (FE-SEM) (JEOL JSM-7001F). The microstructure and grain size of the GO-$TiO_2$ composite were determined using high-resolution transmission electron microscope HRTEM (JEOL JEM 3010) with an accelerating voltage of 300kV. The structural characteristics were investigated using Raman spectroscopy (Raman-LTPL) at $\lambda_{ex}$ = 532 nm, and FT-IR spectroscopy (Nicolet MAGNA 560-FTIR). The electrical conductivity of the samples was measured using the four probe method on CMT-Series (Jandel instrument) at RT, and the elemental compositions of the films were investigated using X-ray photoelectron spectroscopy (XPS), and PHI 5000 VersaprobeII (Ulvac-PHI. Inc.). X-ray diffraction (XRD) pattern of the samples were achieved using Bruker D8 Discover with Cu target of X-ray tube. The wettability of the films was assessed using the face contact-angle meter (Kyowa Interface Science-CA-DT). The water contact angle was measured 5 min after a fixed volume of water droplet was dropped onto the film.

### 2.5 Electrochemical characterization

All electrochemical measurement of cyclic voltammetry, galvanostatic charge/discharge of rGT films were investigated by scanning over the potential range of 0.0 to 1.0 V in an aqueous 1 M $Na_2SO_4$ solution with using potentiostat/galvanostat (Ivium-Stat Technologies compactstat) with the standard three-electrode cell configuration, whereby a platinum wire was used as counter electrode, Ag/AgCl (1M KCl) was used as reference electrode, and an ITO-coated glass was used as current collector. The electrode with an active area of 0.1 $cm^2$ was being exposed to the electrolyte during electrochemical measurements.

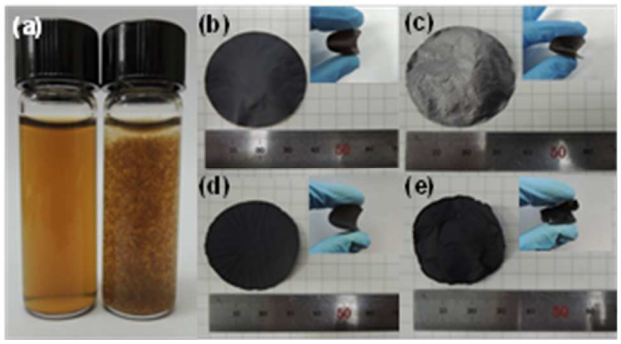


Fig. 2 (a) GO colloidal dispersion (left) and GT composite dispersion (right). Digital images of the freestanding (b) GO, (c) $rGO_{600}$, (d) GT, and (e) $rGT_{600}$ films. Insets display the flexibility of the corresponding films upon bending.

## 3. Results and discussions

### 3.1 Preparation of rGO and rGO-$TiO_2$ freestanding films

A stable homogeneous suspension of GO (Fig. 2a, left) was formed in an aqueous solution owing to the hydrophilic oxygenated functional groups. The thermal hydrolysis of $Ti(SO_4)_2$ in the GO suspension resulted in the

RSC Advances Accepted Manuscript

formation of GT precipitates (Fig. 2a, right). Free standing GT and GO films were obtained by filtering the GT and GO suspension through a cellulose acetate filter, respectively. The as-prepared freestanding films of GT and GO were annealed at 600 °C to synthesize $rGT_{600}$ and $rGO_{600}$, respectively. The resulting films appeared robust and flexible without formation of cracks upon bending, as shown in Fig. 2(b-e).

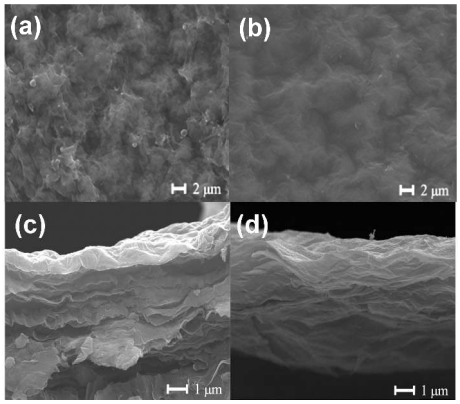


Fig. 3 Surface morphology and cross sectional view of $rGT_{600}$ film (a,c) and $rGO_{600}$ film (b,d).

The surface and cross-sectional morphologies of the $rGT_{600}$ and $rGO_{600}$ films were characterized using FESEM, as shown in Figure 3. The $rGT_{600}$ film featured rough and crumpled morphology, indicating the formation of $TiO_2$ particles that attached homogeneously onto the surface of $rGO_{600}$ sheets (Figure 3a). The $rGO_{600}$ film featured wrinkled morphology typical of pure graphene sheet (Fig. 3b). The cross-sectional images of $rGT_{600}$ (Fig. 3c) revealed a layer-by-layer loosely-packed structure with larger interlayer spacing, compared with that of $rGO_{600}$ film (Fig. 3d). The cross-sectional thickness of $rGT_{600}$ and $rGO_{600}$ were measured to be 7.2 (±0.5) μm and 5.6 (±0.5) μm, respectively. The thickness increase clearly indicated the expansion in the interlayer spacing of $GT_{600}$ sheets due to the $TiO_2$ nanoparticles, which were intercalated into the sheets of rGO sheets. The crumpled structure of $rGT_{600}$ film would generate enlarged pores accessible to the electrolyte ions, as compared to the compact stacked structure of $rGO_{600}$ film.[38]

### 3.2 Material characterization of freestanding rGO and rGT films

The GT films were converted to rGT films by thermal annealing at different temperature (100 - 600 ºC). The effect of the thermal treatment on the reduction degree of GT was investigated using FTIR spectroscopy, as shown in Fig. 4a. The FTIR spectra of the GT composite films showed a strong absorption peak at 600 $cm^{-1}$, which was ascribed to Ti-O-Ti vibration of $TiO_2$ particles formed on the GO flakes.[27] The broad peaks at 3400, 1380, and 1050 $cm^{-1}$ were attributed to O-H, C-OH, and C-O stretching vibrations, respectively, indicating the presence of the epoxide and hydoxyl groups on the GO layers.[39] The peak at 1740 and 1620 $cm^{-1}$ were assigned to C=O stretching of COOH (carboxyl) functional group and aromatic C=C, respectively.[40] After thermal annealing at 600 ºC, the spectra of rGO and rGT films exhibited drastic decrease in almost peaks of the oxygenated functional groups, indicating the complete reduction of GO to rGO.

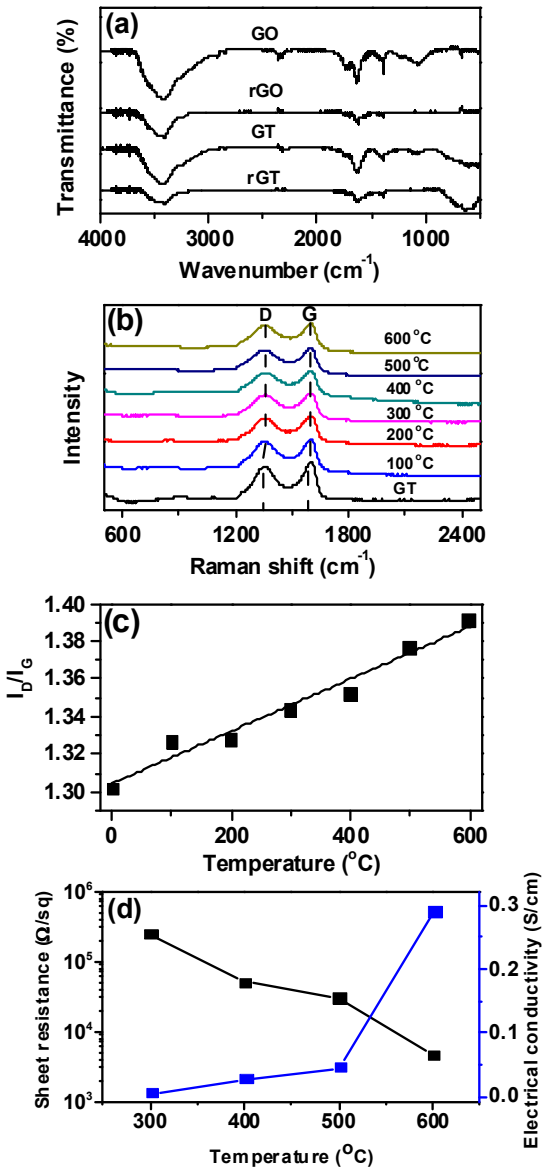


Fig. 4 (a) IR spectra of GO, $rGO_{600}$, GT, and $rGT_{600}$, (b) Raman spectra of GT and rGT films reduced at different temperatures.(c) The plot for the $I_D/I_G$ value of rGT films vs. reduction temperature. (d) Plot of the sheet resistance and electrical conductivity of GT films as a function of the reduction temperature. Note that the sheet resistance of the GT films was measured using a standard four-point probe method.

RSC Advances Accepted Manuscript

Fig. 4b showed the Raman spectra of GT before and after thermal treatment at different temperature (100 – 600 ºC). The characteristic D (1340 $cm^{-1}$) and G (1595 $cm^{-1}$) bands of GO indicate the presence of disordered $sp^3$ and $sp^2$ carbon atoms, respectively. The intensity of D to G ratio ($I_D/I_G$) is widely used to estimate the degree of both the disorder and the crystallite size in graphitic materials.[39,40] The $I_D/I_G$ values of the rGT films increased linearly with increasing annealing temperatures (Fig. 4c), indicating the fact that the oxygenated functional groups were removed more effectively at higher temperature along with increase of the $sp^2$ domains.[43] Furthermore, the sheet resistance of the rGT film prepared at different reduction temperature was measured using four-point probe technique, as shown in Fig. 4d. The films annealed at temperature below 200 ºC showed insulating properties. However, the sheet resistance of the films decreased by about two orders of magnitude from 2.5 x $10^5$ to 4.7 x $10^3$ Ω/sq, when the reduction temperature was increased from 300 to 600 ºC. The electrical conductivity of the rGT films recalculated from the corresponding sheet resistances increased exponentially from the insulating state to 0.29 (±0.03) S/cm, indicating great improvement in the electrical conductivity of the films due to the incorporation of the highly conductive rGO component into the composite rGT-$TiO_2$ electrodes.

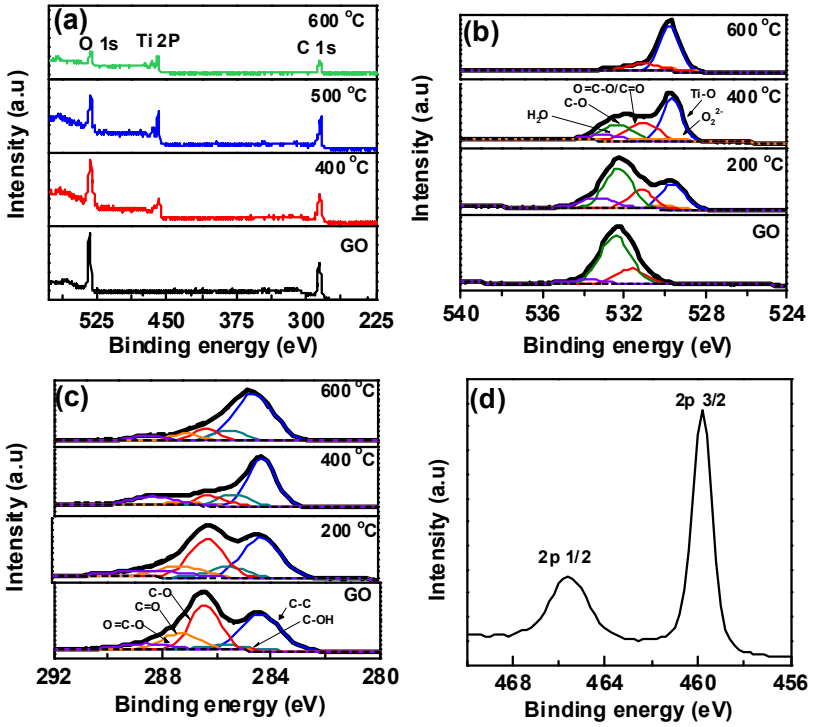


Fig. 5 XPS spectra of GO, $rGT_{200}$, $rGT_{400}$, $rGT_{600}$ films. (a) The survey scan, (b) Comparison of O 1s, (c) Comparison of C 1s, (d) Scaled Ti 2p of $rGT_{600}$ film.

Table 1.The binding energy (eV) and composition (%) of the functional groups comprised in C 1s and O 1s peaks in XPS of the GO and rGT at different reduction temperature.

| Samples | | O 1s | | | | | C 1s | | | | |
|---|---|---|---|---|---|---|---|---|---|---|---|
| | | $H_2O$ | C-O | O=C-O/ C=O | $O_2^{2-}$ | Ti-O | O=C-O | C=O | C-O | C-OH | C-C |
| GO | (eV) | 533.8 | 532.4 | 531.6 | . | . | 288.5 | 287.3 | 286.4 | 285.6 | 284.4 |
| | (%) | (6.4) | (72.6) | (21.0) | | | (7.4) | (16.3) | (34.5) | (5.5) | (36.3) |
| $rGT_{200}$ | (eV) | 533.7 | 532.3 | 531.1 | 530.1 | 529.6 | 288.5 | 287.3 | 286.3 | 285.6 | 284.3 |
| | (%) | (13.5) | (41.9) | (17.5) | (3.9) | (23.2) | (10.3) | (12.1) | (31.3) | (9.5) | (36.8) |
| $rGT_{400}$ | (eV) | 533.7 | 532.4 | 531.7 | 530.3 | 529.9 | 288.5 | 287.2 | 286.4 | 285.5 | 284.4 |
| | (%) | (8.9) | (23.0) | (24.6) | (5.3) | (38.2) | (11.4) | (8.3) | (14.6) | (12.6) | (53.1) |
| $rGT_{600}$ | (eV) | 533.8 | 532.5 | 531.6 | 530.4 | 530.0 | 288.5 | 287.3 | 286.5 | 285.6 | 284.5 |
| | (%) | (1.2) | (1.4) | (25.3) | (6.0) | (66.1) | (12.8) | (6.0) | (9.6) | (13.7) | (57.9) |

RSC Advances Accepted Manuscript

The reduction of GT to rGT films at different temperature was evaluated based on their elemental compositions that were determined using X-ray photoelectron spectroscopy (XPS), and were compared with those of the pure GO. A high-resolution XPS survey scans of the rGT film annealed at different temperature (Fig. 5a) showed three distinct peaks; O 1s (532 eV), C 1s (285 eV) and Ti 2p (460 eV).[27,44,45] These three characteristic peaks were deconvoluted to resolve the individual peaks of the functional groups obtained from the detailed scan. The binding energy (eV) and the relative composition (%) of the functional groups are listed in Table 1 for comparisons. Deconvolution of O1s peak for GO film (Fig. 5b) exhibited three distinguishable peaks, which were assigned to various oxygenated GO functional groups; O=C-O/C=O (531.6 eV), C-O (532.4 eV), and $H_2O$ (533.8 eV).[45] In addition, two additional peaks of Ti-O (529.6 eV) and $O_2^{2-}$ (530.1 eV) were observed from the rGT film.[28,44] A profound reduction in the peak intensity of C-O bonding (532.4 eV) was observed from rGT versus GO films, as the reduction temperature increased to 600 ºC, indicating the elimination of oxygenated functional groups including hydroxyl, carbonyl and carboxyl groups.[45] Furthermore, deconvolution of C1s peak (Fig. 5c) showed characteristic peaks of C-C/C=C (284.4 eV), C-OH (285.6 eV), C-O (286.5 eV), C=O (287.2 eV), and O=C-O (288.8 eV) in the GO and rGT films, indicating the presence of oxygenated functional groups on the GO sheet.[1,25-27,44] The peak intensity of C-O and C=O bonding decreased dramatically, when the reduction temperature was increased to 600 ºC, indicating almost complete removal of the oxygenated functional groups including hydroxyl, epoxy, and carbonyl.[45] The deconvolution of Ti 2p for Ti atom (Fig. 5d) showed two characteristic peaks corresponding to Ti $2p_{3/2}$ (459.4 eV) and Ti $2p_{1/2}$ (465.2 eV). The presence of Ti-O peaks in the GT film before and after thermal treatment implied the high thermal stability of the $TiO_2$ particles.[25]

The morphology and structure of the GO and GT were characterized using HRTEM. A typical wrinkle structure of GO sheet was shown in Fig. S1 (a). $TiO_2$ particles with the average particle size of 5nm were uniformly deposited on the GO sheet with high density (Fig. S1b). The lattice fringe of $TiO_2$ nanoparticle (Fig. S1c) displayed the lattice spacing of the anatase (101) plane of $TiO_2$ to be 0.35 nm, which agreed well with the lattice spacing of $TiO_2$ reported previously.[25,46] The crystalline structures of GO and rGT at different temperature were determined by powder X-ray diffraction measurement, as shown in Fig. S2. The XRD pattern of GO showed a pronounced diffraction peak at 2θ of 12°, which was attributed to (002) plane of GO.[47] The diffraction peak of GT and rGT heated at different temperature were observed at 2θ of 25°, 48° and 55°, corresponding to (101), (200), and (105) planes of anatase titania, respectively.[25] By increasing the temperature to 600 °C, the GO peak in rGT at 12° disappeared completely and a new broad peak appeared at 2θ of 22°, indicating reduction of GO to rGO.[27]

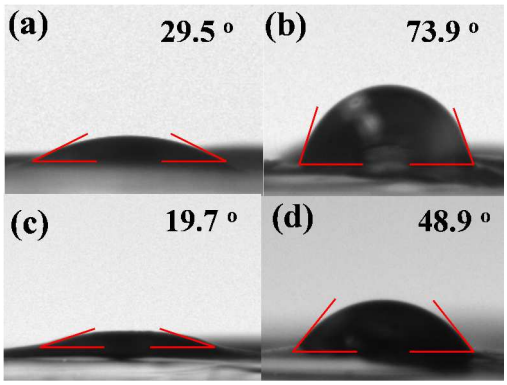


Fig. 6 Water contact angle of (a) GO, (b) $rGO_{600}$, (c) GT, and (d) $rGT_{600}$

The wettability of an electrode is an additional critical factor to decide the accessibility of aqueous electrolytes into the electrode. Thus, the wettability of $rGO_{600}$ and $rGT_{600}$ film surfaces was assessed based on the stationary water contact angle. The water contact angle (29.5º) of GO drastically increased to 73.9º as reduced to $rGO_{600}$ after thermal reduction at 600 ºC, indicating the increased surface hydrophobicity, as shown in Figure 5. However, the contact angle (19.7º) of GT increased not strongly for $rGT_{600}$ (48.9º) compared to the case of the GO and $rGO_{600}$. The enhanced water wettability of both the GT and $rGT_{600}$ electrodes could be ascribed to the involvement of the hydrophilic component $TiO_2$ in addition to the increased film porosity, which was attributed to the crumpled and $TiO_2$-intercalated structure of the GT films.

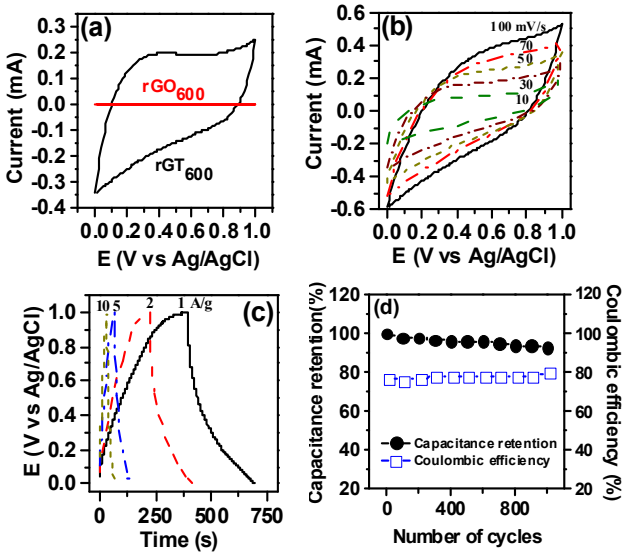


Fig. 7 (a) Comparison of CV curve for $rGO6_{00}$ and $rGT_{600}$. (b) CV curve of $rGT_{600}$ electrodes at various scan rates (c) Galvanostatic charge/discharge curves of $rGT_{600}$ electrodes

RSC Advances Accepted Manuscript

at various current densities (d) cycling stability and coulombic efficiency of $rGT_{600}$ electrode.

### 3.3 Electrochemical properties of the rGT electrode in a three-electrode setup

The capacitive performance of the rGTx electrode was evaluated using cyclic voltammetry (CV) and galvanostatic charge/discharge technique in 1 M $Na_2SO_4$ aqueous electrolyte. The nearly-rectangular CV curve of $rGT_{600}$ electrode appeared relatively larger compared to that of the $rGO_{600}$ electrode, indicating the higher capacitive performance, as shown in Fig. 7a. The improved capacitive performance of the $rGT_{600}$ electrode versus the $rGO_{600}$ electrode could be attributed to the improved hydrophilicity of the $rGT_{600}$, which enhanced the accessibility of the aqueous electrolyte into the $rGT_{600}$ electrode. The area under the CV curve of the $rGT_{600}$ electrode (Fig. 7b) increased with the scan rate ranging from 10 to 100 mV/s. However, the CV curve was slightly distorted due to the increase in the electrode resistance at a high scan rate of 100 mV/s.[48] Fig. 7c showed the charge-discharge curves of the electrode, which was measured at various current densities ranging from 1 from 10 A/g within the potential range of 0 – 1 V. Asymmetrical behavior of the charge-discharge curve was observed for the electrode at low region of current densities, which can be ascribed to the redox reaction of $TiO_2$.[27] However, the capacitive performance of the $rGT_{600}$ electrode decreased upon increasing the scan rate and the current density, due to the high electrical and ionic resistances of the electrode at high charging-discharging rates. At low scan rates, nearly the entire electrode is accessible to the diffusion-controlled intercalation/deintercalation of electrolyte ions, resulting in the improved specific capacitance of the electrode.[49,50]

The specific capacitances of rGT electrode were determined from the galvanostatic discharge curve as a function of the reduction temperature (Fig. 7d), according to the following equation (1)[48]

$$C_s = (I \cdot \Delta t)/(m \cdot \Delta E) \quad (1)$$

where $I$ is the current loaded, $\Delta t$ is the discharge time, $\Delta E$ is the potential range after IR drop during discharge process, and m is the mass of the working electrode of rGT. The maximum specific capacitance of the rGT electrode annealed at 600 ºC was calculated to be 286 F/g. The resulted value is much higher, compared to a closely related electrode like $TiO_2$-graphene nanocomposite hydrogel (175 F/g at 1 A/g), which was prepared using hydrothermal approach reported in a previous literature.[1] The improvement of specific capacitance by the rGT was attributed to the loosely-stacked layered structure of the rGT electrode, in which the $TiO_2$ nanoparticles was formed directly on the graphene sheets,[34] compared to the bulk nanocomposite of $TiO_2$-graphene hydrogel electrode.[1] The good contact between the two materials can be beneficial for rapid charge transfer by electron injection from $TiO_2$ into the graphene sheets. Furthermore, the average energy density (E, Wh/Kg) and power density (P,W/kg) of the $rGT_{600}$ electrode were calculated using the following equation (2) and (3):[27]

$$E = 0.5 \cdot C_s \cdot (\Delta V)^2 \quad (2)$$

$$P = E/t \quad (3)$$

where the $C_s$ is the specific capacitance of the electrode material (F/g), $t$ is the discharge time of the charge/discharge curve, and $\Delta V$ is the potential window. The average energy density and power density of the $rGT_{600}$ electrode were calculated to be 39.7 Wh/kg and 472 W/kg at 1 A/g, respectively. The rGT electrode showed a tendency for the area under CV and the charge-discharge curves to increase upon the reduction temperature for rGT, which increased from 300 to 600 ºC, as shown in Fig. S3 (a) and (b) in supporting information (SI). The long-term cycling stability and coulombic efficiency of $rGT_{600}$ electrode in 1.0 M $Na_2SO_4$ aqueous electrolyte (Fig. 7d) were evaluated using galvanostatic charge/discharge measurement at 1 A/g for 1000 cycles in the potential range of 0 to 1V. The $rGT_{600}$ electrode exhibited excellent cycling stability with 93% capacitance retention after 1000 continuous charge/discharge cycles and a coulombic efficiency of almost 80%.

## 4. Conclusion

In summary, we have fabricated a highly flexible freestanding film electrode composed of graphene and $TiO_2$ using a simple vacuum-assisted filtration, resulting in the aligned stacking structure of GO/$TiO_2$ layers. The $TiO_2$ intercalated into GO layers, led to the formation of crumpled GO/$TiO_2$ films, in which large pores accessible to electrolytes would be generated. The electrical conductivity of an electrode is a critical factor to decide the level of energy storage in supercapacitor. The conductivity of the hybrid rGT electrode strongly relies on the reduction state of GO, which was investigated as a function of the annealing temperature. The reduction state of GO in the hybrid electrode was evaluated using RAMAN and XPS, as the annealing temperature was ranged from 100 to 600 ºC. From RAMAN spectra of the rGT films, the $I_D/I_G$ values increased linearly with increasing annealing temperatures from 100 to 600 ºC, indicating the fact that the oxygenated functional groups were removed more effectively at higher temperature along with increase of the $sp^2$ domains. In addition, the peak intensity of C-O and C=O bonding, which was determined from XPS of rGT films, decreased dramatically, as the reduction temperature was increased to 600 ºC, indicating almost complete removal of the oxygenated functional groups including hydroxyl, epoxy, and carbonyl. The sheet resistances of the rGT films decreased exponentially by two

RSC Advances Accepted Manuscript

orders of magnitude from $2.5x10^5$ to $4.7x10^3$ Ω/sq, as the reduction temperature of GT (to rGT) increased from 300 to 600 ºC. These results indicated that the thermal reduction of the GT at 600 ºC was an optimal condition for the resulting film electrode, which is conductive, robust, and flexible. The $rGT_{600}$ film electrode exhibited the specific capacitance of 286 F/g at the 1 A/g, which is much higher than the closely related electrode, $TiO_2$-graphene nanocomposite hydrogel (175 F/g at 1 A/g), which was prepared using hydrothermal approach reported in a previous literature.[1] The long-term cycling stability of $rGT_{600}$ electrode in 1.0 M $Na_2SO_4$ aqueous electrolyte exhibited excellent cycling stability with 93% capacitance retention after 1000 continuous charge/discharge cycles at 1 A/g under the potential range of 0 to 1V. The hybrid $rGT_{600}$ electrode exhibited the excellent electrochemical properties, which are required for the development of advanced micro-size and flexible electrodes in energy storage devises.

## Acknowledgements

This research was supported by the Research Grant of Incheon National University in 2013, and Basic Science Research Program through the National Research Foundation of Korea (NRF) funded by the Ministry of Education, Science and Technology (20110015807).

## Notes and references

[a] Department of Chemistry, Incheon National University, 119 Academy-ro Yeonsu-gu, Incheon 406-772, Republic of Korea
[b] Research Institute for Natural Sciences, Incheon National University, 119 Academy-ro Yeonsu-gu, Incheon 406-772, Republic of Korea
E-mail: hong5506@incheon.ac.kr
TEL: 82-32-835-8234, FAX. 82-32-835-0762

† Electronic Supplementary Information (ESI) available: The CV curve and galvanostatic charge/discharge curve of rGT electrode reduced at different temperature. See DOI: 10.1039/b000000x/

1. Z. Zhang, F. Xiao, Y. Guo, S. Wang, Y. Liu, *ACS Appl. Mater. Interfaces*, 2013, **5**, 2227-2233.
2. H. R. Byon, S. W. Lee, S. Chen, P. T. Hammond, S. H. Yang *Carbon*, 2011, **49** 457-467.
3. J. B. Goodenough, H. D. Abruña, M. V. Buchanan, *Report of the basic energy sciences workshop on electrical energy storage*, US department of Energy, Washington, 2007.
4. P. Simon, Y. Gogotsi, Nat. *Mater*., 2008, **7**, 845-854.
5. Z. S. Wu, D. W. Wang, W. Ren, J. Zhao, G. Zhou, F. Li, H. M. Cheng, *Adv. Funct. Mater*., 2010, **20**, 3595-3602.
6. L. Lai, H. Yang, L. Wang, B. K. The, J. Zhong, H. Chou, L. Chen, W. Chen, Z. Shen, R. S. Ruoff, J. Lin, *ACS Nano*, 2012, **6**, 5941-5951.
7. M. Inagaki, H. Konno, O. Tanaike, *J. Power Sources*, 2010, **195**, 7880-7903.
8. A. G. Pandolfo, A. F. Hollenkamp, *J. Power Sources*, 2006,**157**, 11-27.
9. C. C. Hu, T. W. Tsou, *Electrochem. Commun*., 2002, **4**, 105-109.
10. L. L. Zhang, S. Zhao, X. N. Tian, X. S. Zhao, *Langmuir*, 2010, **26** , 17624-17628.
11. A. K. Saker, J. D. Hong, *Langmuir*, 2012, **28**, 12637-12646.
12. J. P. Ferraris, M. M. Eissa, I. D. Brotherston, D. C. Loveday, *Chem. Mater*., 1998, **10**, 3528-3535.
13. A. Pendashteh, M. F. Mousavi, M. S. Rahmanifar, *Electrochim. Acta*., 2013, **88**, 347-357.
14. Y. Chen, X. Zhang, D. Zhang, P. Yu, Y. Ma, *Carbon*, 2011, **49**, 573-580.
15. M. J. Allen, V. C. Tung, R. B. Kaner, *Chem. Rev*., 2010, **110** , 132-145.
16. D. R. Dreyer, S. Park, C. W. Bielawski, R. S. Ruoff, *Chem, Soc, Rev.*, 2010, **39**, 228-240.
17. S. Pei, H. M. Cheng, *Carbon*, 2010, **50**, 3210-3228.
18. S. Stankovich, D. A. Dikin, G. H. B. Demmett, K. M. Kohlhaas, E. J. Zimney, E. A. Stach, R. D. Piner, S. T. Nguyen, R. S. Ruoff, *Nature*, 2006, **442**, 282-286.
19. W. H. Khoh, J. D. Hong, *Colloids and Surfaces A: Physicochem. Eng. Aspects*, 2013, **436**, 104– 112.
20. Y. Zhu, S. Murali, W. Cai, X. Li, J. W. Suk, J. R. Potts, R. S. Ruoff, *Adv. Mater*., 2010, **22**, 3906-3924.
21. Z. F. Li, H. Zhang, Q. Liu, L. Sun, L. Stanciu, J. Xie, *ACS Appl. Mater. Interfaces*., 2013, **5**, 2685-2691.
22. Q. WU, Y. Xu, Z. Yao, A. Liu, G. Shi, *ACS Nano*, 2010, **4**, 1963-1970.
23. J. Yan, T. Wei, B. Shao, F. Ma, Z. Fan, M. Zhang, C. Zheng, Y. Shang, W. Qian, F. Wei, *Carbon*, 2010, **48**, 1731-1737.
24. C. Xiang, M. Li, M. Zhi, A. Manivannan, N. Wu, *J. Mater. Chem*., 2012, **22** 19161-19167.
25. M. S. A. S. Shah, A. R. Park, K, Zhang, J. H. Park, P. J. Yoo, *ACS Appl. Mater. Interfaces*, 2012, **4**, 3893-3901.
26. D. Wang, X. Li, J. Chen, X. Tao, *Chem. Eng. J.,* 2012, **198-199**, 547-554.
27. A. Ramadoss, S. J. Kim, *Carbon*, 2013, **63**, 434-445.
28. M. C. Yang, Y. Y. Lee, B. Xu, K. Powers, Y. S. Meng, *J. Power Sources*, 2012, **207**, 166-172.
29. A. K. Mishra, S. Ramaprabhu, *J. Phys. Chem. C*, 2011, **115**, 14006-14013.
30. J. Liu, J. Sun, L. Gao, *J. Phys. Chem*. C, 2010, **114**, 19614-19620.
31. J. Liu, J. Sun, L. Gao, *Nanoscale*, 2011, **3**, 3616-3619.
32. J. Liu, L. Zhang, H. B. Wu, J. Lin, Z. Shen, X. W. Lou, *Energy Environ. Sci*., 2014, **7**, 3709-3719.
33. Y. Xu, Z. Lin, X. Huang, Y. Liu, Y. Huang, X. Duan, ACS Nano, 2013, 7, 4042-4049.
34. M. Dahl. Y. Liu, Y. Yin, *Chem. Rev*., 2014, **114**, 9853-9889.
35. L. Tian, P. Anilkumar, L. Cao, C. Y. Kong, M. J. Meziani, H. Qian, L. M. Veca, T. J. Thorne, K. N. Tackett, T. Edwards, Y. P. Sun, *ACS Nano*, 2011, **5**, 3052-3058.
36. C. Xu, A. Cui, Y. Xu, X. Fu, *Carbon*, 2013, 62, 465-471.
37. C. Xu, A. Cui, Y. Yuan, Z. Chen, R. Yuan, X. Fu, *J. Mater. Sci*., 2013, **48**, 3428-3435.
38. Y. Li, J. Wang, X. Li, D. Geng, R. Li, X. Sun, *Chem. Commun*., 2011, **47**, 9438-9440.

RSC Advances Accepted Manuscript

39. Y. Si, E. T. Samulski, *Nano Lett.,* 2008, **8**, 1679-1682.
40. M. Acik, G. Lee, C. mattevi, M. chhowalla, K. Cho, Y. J. Chabal, *Nat. Mater*., 2010, **9**, 840-845.
41. H. Liu, L. Zhang, Y. Guo, C. Cheng, L. Yang, L. Jiang, G. Yu, W. Hu, Y. Liu, D. Zhu, *J. Mater. Chem. C*, 2013, **18**, 3104-3109.
42. G. K. Ramesha, S. Sampath , *J. Phys. Chem. C*, 2009, **113**, 7985-7989.
43. A. C. Ferrari, J. Robertson, *Phys. Rev. B,* 2000, **61**, 14095-14107.
44. F. Dong, S. Guo, H. Wang, X. Li, Z. Wu, *J. Phys. Chem. C*, 2011, **115**, 13285-13292.
45. B. H. Wee, J. D. Hong, Adv. *Func. Mater*., 2013, **23**, 4657-4666.
46. Y. Liang, H. Wang, H. S. Casalongue, Z. Chen, H. Dai, *Nano Res*., 2010, **3**, 701-705.
47. B. Y. Xia, H. B. Wu, J. S. Chen, Z. Wang, X. Wang, X. W. Lou, *Phys. Chem. Chem. Phys*, 2012, *14*, 473-476.
48. W. W. Liu, X. B. Yan, J. W. Lang, C. Peng, Q. J. Xue, *J. Mater. Chem*., 2012, **22**, 17245-17253.
49. Y. Wang, Z. Shi, Y. Huang, Y. Ma, C. Wang, M. Chen, Y. Chen, *J. Phys. Chem*., 2009, **113**, 13103-13107.
50. V. Khomenko, E. R. Pinero, E. Frackowiak, F. Beguin, *Appl. Phys. A*., 2006, **82**, 567-573.

RSC Advances Accepted Manuscript